

# 1    The Lightning Differential Space Framework: Multiscale Analysis 2    of Stroke and Flash Behavior

3  
4

5    Yuval Ben Ami<sup>1</sup>, Orit Altaratz<sup>1</sup>, Yoav Yair<sup>2</sup>, Ilan Koren<sup>1</sup>

6    <sup>1</sup>Department of Earth and Planetary Sciences, The Weizmann Institute of Science, Rehovot, 7610001, Israel.

7    <sup>2</sup>School of Sustainability, Reichman University, Herzliya, 4610101, Israel.

8

9    *Correspondence to:* Ilan Koren (ilan.koren@weizmann.ac.il)

10

11    **Abstract.** Lightning flashes play a key role in the global electrical circuit, serving as markers of deep convection and  
12    indicators of climate variability. However, this field of research remains challenging due to the wide range of physical  
13    processes and spatiotemporal scales involved.

14    To address this challenge, this study utilizes the Lightning Differential Space (LDS), which maps lightning stroke  
15    intervals onto a parameter space defined by their temporal and spatial derivatives.

16    Using data from the Earth Networks Total Lightning Network (ENTLN), we analyze the Number Distribution LDS  
17    clustering patterns across specific seasons in three climatically distinct regions: a tropical rainforest region (Amazon), a  
18    subtropical marine environment (Eastern Mediterranean Sea), and a mid-latitude continental region (Great Plains in the  
19    U.S.). The LDS reveals a robust clustering topography composed of “allowed” and “forbidden” interval ranges, which  
20    are consistent across regions, while shifts in cluster position and properties reflect the underlying regional meteorological  
21    conditions.

22    As an extension of the LDS framework, we introduce the Current Ratio LDS, a new diagnostic for identifying flash  
23    initiation by mapping the ratio of peak currents between successive strokes into the LDS coordinate space. This space  
24    reveals a spatiotemporal structure that enables a clearer distinction between local and regional scales. It also reveals a  
25    distinct cluster, suggesting a possible teleconnection between remote strokes, spanning tens to hundreds of kilometers.

26    Together, the Number Distribution LDS and the novel Current Ratio LDS provide a scalable, data-driven framework for  
27    analyzing and interpreting large datasets of CG lightning activity. This approach strengthens the ability to characterize  
28    multiscale lightning behavior, offers a framework for evaluating model representations of stroke and flash processes, and  
29    provides a basis for developing diagnostics relevant to operational monitoring and forecasting of lightning activity.

## 30    1. Introduction

31    Cloud-to-Ground (CG) lightning flashes play a significant role in the global atmospheric electric circuit (Siingh et al.,  
32    2007), making it essential to understand their properties and driving mechanisms. In addition, studying CG flashes is  
33    important for improving safety measures, as they pose severe hazards to life and infrastructure (Yair, 2018).

34    Thunderclouds are the building blocks of deep cloud systems. The size of a single Cumulonimbus typically ranges from  
35    a few to a few tens of kilometers, depending on the season and location (Cotton et al., 2011). Their lightning production  
36    rate varies between one flash every few seconds to one every few minutes, for a total duration ranging from a few minutes

37 up to  $\sim$ 1 h (Dwyer and Uman, 2014). The lightning production rate and total duration of a thundercloud's electrical  
38 activity depend on dynamic and microphysical processes, such as the updraft magnitude, the depth of the mixed-phase  
39 region, and the fluxes of liquid water, graupel, and ice mass within the cloud (Deierling and Petersen, 2008; Deierling et  
40 al., 2008). A major part of CG flashes (mainly negative ones) consists of multi-stroke flashes, transferring charge to the  
41 ground through several return strokes, some of which may follow different channels and contact the ground within a  
42 radius of  $\sim$ 10 km (Dwyer and Uman, 2014). The gaps between strokes are generally a few tens of milliseconds, and a CG  
43 flash has a total duration of 0.5–1 s. Studies have statistically shown that the first return stroke in a lightning flash generally  
44 has a stronger peak current than subsequent strokes (Chowdhuri et al., 2005; Poelman et al., 2013; Diendorfer et al.,  
45 2022). Positive CG flashes usually consist of a single return stroke and have a higher peak current compared to negative  
46 ones (Rakov, 2003).

47 Many previous studies have examined the spatiotemporal properties of strokes and flashes and their relation to the micro  
48 and macrophysical properties of thunderclouds (e.g., Mattos and Machado, 2011; Strauss et al., 2013). These properties  
49 depend on geographic location, season, and type of convective system.

50 Observational studies also show that when thunderclouds cluster into an organized system, distinct spatial and temporal  
51 lightning patterns can emerge. For example, in the case of Mesoscale Convective Systems (MCS), this can include a high  
52 rate of cloud-to-ground (CG) flashes, a large horizontal extent of flashes, a bipolar pattern of ground contact points, and  
53 other characteristics (MacGorman and Rust, 1998). On a larger scale, several studies suggest a coupling mechanism  
54 between widely separated thunderclouds, leading to synchronized lightning activity patterns (i.e., teleconnection; Mazur,  
55 1982; Vonnegut et al., 1985; Yair., et al 2006, 2009a).

56 Because lightning behavior depends on thunderstorm characteristics and environmental conditions, robust  
57 characterization of stroke and flash properties requires large datasets that cover many storms. Lightning detection  
58 networks are valuable tools for this purpose, as they provide years of measurements collected over both land and ocean.

59 With advancements in measurement technology and retrieval algorithms, there is a growing interest in developing analysis  
60 techniques that can extract new physical insights from existing long-term lightning network data. Traditional approaches  
61 to processing lightning-network data typically begin by grouping individual strokes into flashes using predefined spatial–  
62 temporal thresholds, a strategy employed in most operational flash algorithms. These approaches and their sensitivities  
63 are reviewed in San Segundo et al. (2020). In contrast, the Lightning Differential Space (LDS) framework provides a  
64 continuous, data-driven representation of stroke intervals without imposing a particular grouping scheme, allowing the  
65 multiscale structure of electrical activity to emerge directly from the observed data.

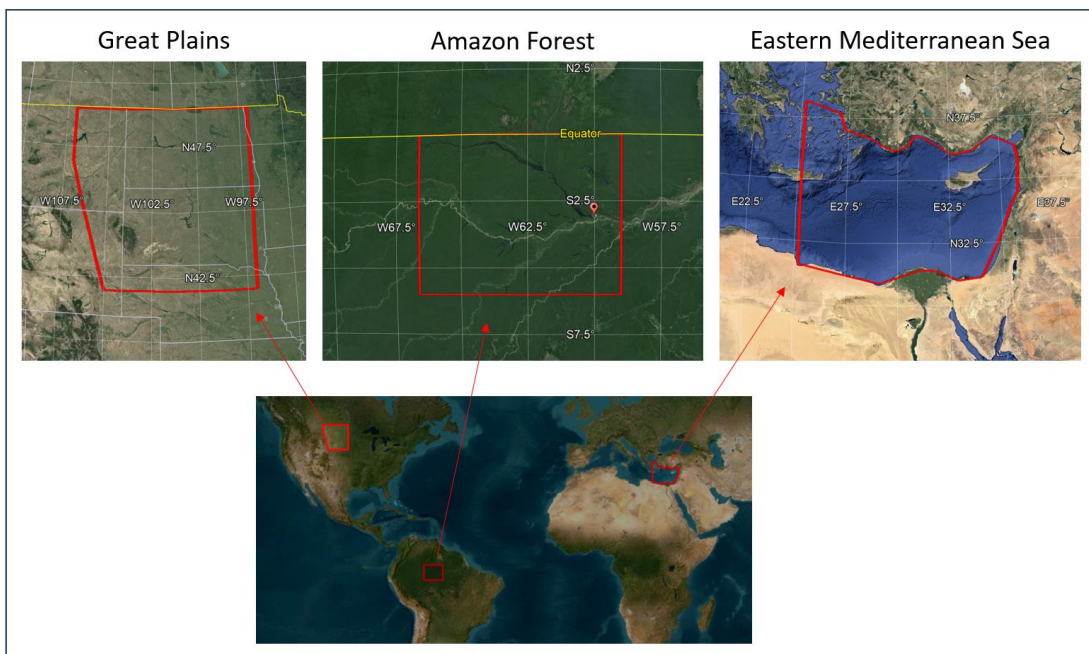
66 Here, we extend the investigation of Ben Ami et al. (2022), who presented a unique differential space that reveals common  
67 properties of time and distance intervals between successive strokes and used it to characterize CG flash activity on both  
68 thundercloud and cloud-system scales. Their work focused on winter Cyprus Lows in the Eastern Mediterranean,  
69 analyzing  $\sim$ 50,000 CG strokes that were measured by the Israel Lightning Location System (ILLS, Katz and Kalman,  
70 2009), and introduced the LDS as a novel data-driven diagnostic framework to differentiate between electrical events  
71 across a wide range of spatial and temporal scales.

72 In this study, we expand this investigation to three regions of interest (ROI), representing different climatic regimes, using  
73 CG data collected by a global lightning detection network with a larger dataset per region. Beyond extending the Number  
74 Distribution LDS to new environments, we introduce the Current Ratio LDS (section 2.3), a new diagnostic framework  
75 for identifying flash initiation intervals based on peak current sequencing.

76 **2. Data and Methods**

77 **2.1. Regions and Seasons**

78 The three ROIs are (a) the Amazon ( $0^{\circ}$ - $6^{\circ}$ S;  $66.6^{\circ}$ W- $59^{\circ}$ W), representing the tropics, (b) the Eastern Mediterranean Sea  
 79 ( $31^{\circ}$ N- $35^{\circ}$ N;  $25^{\circ}$ E- $35.5^{\circ}$ E), representing the subtropics, and (c) the northern part of the U.S. Great Plains ( $42^{\circ}$ N- $49^{\circ}$ N;  
 80  $\sim 106^{\circ}$ W- $97^{\circ}$ W), representing the mid-latitudes (Fig. 1). These ROIs were selected because (a) they represent three distinct  
 81 climate regimes. Accordingly, we chose a few key parameters for general characterization of the atmospheric conditions:  
 82 the Convective Available Potential Energy (CAPE), freezing-level height, and mixed-phase layer depth (estimated here  
 83 as the difference between the cloud-top height and the freezing level). These parameters have been shown in previous  
 84 works to be highly correlated with the charge generation and flash rates in thunderstorms (Deierling and Petersen, 2008;  
 85 Carey and Rutledge, 2000; Williams et al., 2002), (b) they exhibit intense seasonal lightning activity (Oda et al., 2022;  
 86 Altaratz et al., 2003; Jiang et al., 2006; Kaplan et al., 2022), and (c) the ROIs are characterized by low-relief surface  
 87 conditions that minimize local orographic triggering of convection, so that large-scale dynamics primarily influence the  
 88 electrical activity. Using the large ENTLN datasets, we analyze and compare the electrical activity in these three regions.



89

90 Figure 1: Maps marking the study regions (© Google Maps 2015). The Amazon is bounded between  $0^{\circ}$ - $6^{\circ}$ S and  $66.6^{\circ}$ W- $59^{\circ}$ W, the  
 91 Great Plains are bounded between  $42^{\circ}$ N- $49^{\circ}$ N, and  $\sim 106^{\circ}$ W- $97^{\circ}$ W, and the Eastern Mediterranean Sea lies approximately between  
 92  $31^{\circ}$ N- $35^{\circ}$ N and  $25^{\circ}$ E- $35.5^{\circ}$ E.

93 **2.1.1 The Amazon (Sep.–Nov.)**

94 During the wet season, lightning activity reaches its annual peak, as the Intertropical Convergence Zone migrates  
 95 southward (Nobre et al., 2009), creating a belt of low pressure. At the same time, the upper levels are influenced by the  
 96 Bolivian High (Molian, 1993). Convection is driven by local instability and moisture supplied by the forest (Wright et  
 97 al., 2017). Additionally, low-level easterly winds transport humidity from the ocean inland, further supporting the  
 98 development of intense convection and electrical activity. Other synoptic systems that support thunderstorm activity  
 99 during the wet season include the South American Monsoon System (Williams et al., 2002) and the South Atlantic  
 100 Convergence Zone, a quasi-stationary band of deep clouds extending from the Amazon Basin southeastward (Carvalho  
 101 et al., 2004). During this season deep mixed-phase thunderclouds develop over the Amazon, with typical cloud-top height  
 102 exceeding 15 km and a freezing level located around 5 km (Harris et al., 2000; Collow et al., 2016). CAPE typically has  
 103 moderate values around  $1000 \text{ J kg}^{-1}$  during most of the season (Williams et al., 2002; Riemann-Campe et al., 2009) with

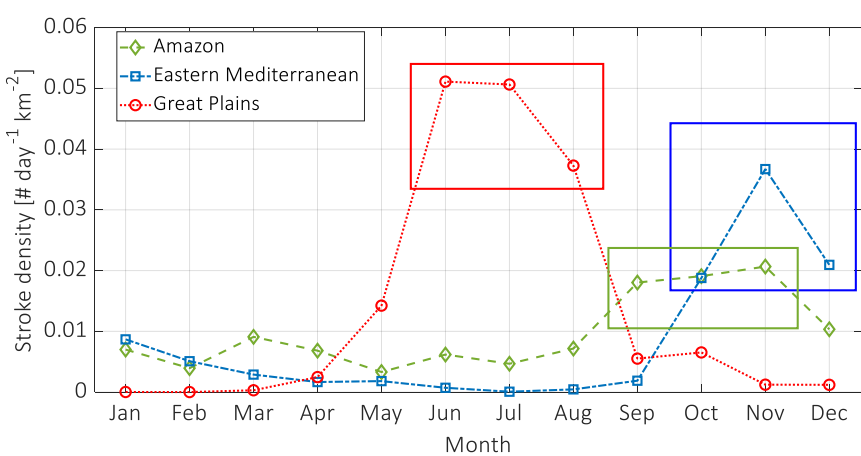
104 maximum values of up to  $\sim 4000 \text{ J kg}^{-1}$  on rare occasions (Giangrande et al., 2017), conditions that support intense  
105 electrical activity (Williams et al., 2002; Andreae et al., 2004).

106 **2.1.2 The Eastern Mediterranean Sea (Oct.–Dec.)**

107 The most intense electrical activity in this region occurs during the boreal autumn and winter, driven mainly by mid-  
108 latitude cyclones. In these systems, continental cold air masses from Europe are advected toward the Mediterranean. As  
109 they propagate eastward over the relatively warm sea, their moisture content increases, and the air masses become  
110 unstable. The low-pressure center is usually located near Cyprus, commonly referred to as a Cyprus Low (Shay-El and  
111 Alpert, 1991). Thunderclouds develop over the sea and near the coasts along cold fronts and post-frontal regions. A less  
112 frequent system is the Red Sea Trough (Ziv et al., 2005; Shalev et al., 2011), originating from the African monsoon over  
113 the Red Sea. When accompanied by an upper-level trough, it can support intense electrical activity over the Eastern  
114 Mediterranean Sea and neighboring countries, often leading to severe flooding. In contrast to the very deep convection in  
115 tropical or summertime mid-latitude environments, autumn and winter storms in this region have a relatively shallow  
116 mixed-phase layer and exhibit low freezing-level heights. Cloud tops are between 7–11 km, with the highest values  
117 typically occurring at the beginning of the season (Altaratz et al., 2001; Yair et al., 2009b), and the freezing level is at  
118  $\sim 2\text{--}3 \text{ km}$  (Altaratz et al., 2001). The CAPE values are modest, typically between few hundreds and  $1000 \text{ J kg}^{-1}$   
119 characteristic of cold-season marine convection (Ben Ami et al., 2015).

120 **2.1.3 The Northern Great Plains (Jun.–Aug.)**

121 During this time of year, this region is part of the corridor for passing MCSs, which are large clusters of thunderstorms  
122 (Tuttle and Davis, 2006). MCSs often develop or intensify during the night, and typically form along fronts (Ziegler and  
123 Rasmussen, 1998; Maddox et al., 1986) or drylines, the boundary between moist air from the Gulf of Mexico and dry air  
124 from the desert Southwest (Scaff et al., 2021). MCSs can be sustained by a low-level jet, which peaks after sunset and  
125 drives a southerly wind that supplies warm and humid air from the Gulf of Mexico (Higgins et al., 1997). Summer  
126 convection in the Great Plains is typically associated with CAPE values of  $\sim 1000\text{--}2500 \text{ J kg}^{-1}$  (Gizaw et al., 2021;  
127 Riemann-Campe et al., 2009), along with deep mixed-phase thunderclouds with cloud-top height of  $\sim 18 \text{ km}$  (Setvák et  
128 al., 2010). The freezing level is located at  $\sim 5 \text{ km}$  (Wiens and Suszcynsky, 2006) and there is usually strong vertical wind  
129 shear, reflecting the thermodynamic and dynamical structure that favors the development of long-lived, highly electrified  
130 MCSs (Higgins et al., 1997; Tuttle and Davis, 2006). These conditions contrast with the weak-shear, moist-tropical  
131 environment of the Amazon and define a distinct midlatitude convective regime.



132

133 Figure 2: A histogram of the daily CG density (number of strokes per  $\text{day}^{-1} \text{km}^{-2}$ ) per month during 2020–2021. The selected months  
134 for analysis are indicated, based on the highest stroke density for each ROI.

135 **2.2. Measurement System and Data**  
 136 The CG stroke data used in this study were primarily retrieved by the ENTLN (Zhu et al., 2022). This network comprises  
 137 more than 1,500 wideband (1 Hz-12 MHz) sensors, deployed worldwide. Based on the detected electric-field waveform  
 138 and the time-of-arrival technique, the network estimates the pulse type (CG or intra-cloud; IC), ground-contact point,  
 139 time of impact, peak current, and polarity.

140 Based on analyses of rocket-triggered and natural flashes, the reported CG stroke detection efficiency and classification  
 141 accuracy (estimated over the U.S.) are at least 96% and 86%, respectively. The median location error is 215 m, and the  
 142 absolute peak current error is 15%. A detailed description of the network performance can be found in Zhu et al. (2022).

143 In this study, we use CG stroke data. For each ROI, we focus on the specific season with the highest stroke density within  
 144 2020–2021 (Fig. 2, Table 1), ensuring that the LDS analysis is based on a large and representative sample of CG activity  
 145 for each region. The total analyzed dataset includes 8,337,978 strokes, detected over 182 days in the Amazon, 118 days  
 146 in the Eastern Mediterranean, and 175 days in the Great Plains during the selected seasons.

147 To support and validate our ENTLN results, we use an additional CG dataset, measured by another lightning network,  
 148 the Israeli Lightning Location System. At the time, the ILLS network included eight sensors, sensitive to the electric  
 149 and/or magnetic fields (Katz and Kalman, 2009). It detected 251,393 CGs over 265 stormy days with diverse synoptic  
 150 conditions, during Oct.–Dec. of 2004–2008 and 2010. Our ILLS dataset does not overlap with the ENTLN period (2020–  
 151 2021), but it covers similar months of the year and hence a similar type of synoptic systems, and can be used for validation.  
 152 Due to the detection limits of the ILLS, the validation of the ENTLN analysis against the ILLS data was done in a different  
 153 area covering 250 km from the network center over the Eastern Mediterranean Sea and the adjacent land (Fig. S1). This  
 154 ILLS dataset was used in the previous work by Ben Ami et al. (2022).

155 *Table 1. Season, study area [km<sup>2</sup>], total number of analyzed days (with detected CG flashes), total number of analyzed hours, total  
 156 number of detected CG strokes, number of strokes in clusters A, B+C, and D, and estimated flash density per ROI. (\*Estimated from  
 157 the ratio between the number of intervals B+C+1 to the area and the number of days).*

158

	Amazon	Eastern Mediterranean	Great Plains	Total
<b>Season</b>	Sep.-Nov.	Oct.-Nov.	Jun.-Aug.	-
<b>Area [km<sup>-2</sup>]</b>	563,270	566,010	562,730	<b>1,692,010</b>
<b># of days</b>	182	118	175	<b>475</b>
<b>Number of hours [#]</b>	3,740	1,979	2,854	<b>8,573</b>
<b>Number of CGs</b>	1,974,302	1,790,482	4,573,194	<b>8,337,978</b>
<b>Number of intervals in A [#]</b>	674,538	863,374	869,395	<b>2,407,307</b>
<b>Number of intervals in B+C [#]</b>	1,282,533	894,543	3,642,374	<b>5,819,450</b>
<b>Number of intervals in D [#]</b>	17,230	32,564	61,424	<b>111,221</b>
<b>Flash density [# km<sup>-2</sup> day<sup>-1</sup>]*</b>	0.013	0.013	0.037	-

159

160 **2.3. Method**  
 161 The CG stroke data were sorted by the time of ground impact. Next, the time (dT) and distance (dR) intervals between  
 162 consecutive strokes were calculated by subtracting the detection times and computing the distance between the  
 163 geographical coordinates of each stroke pair. The number of events per interval range was projected onto a two-  
 164 dimensional differential space, defined by dR and dT, termed the Lightning Differential Space (LDS), hereafter referred  
 165 to as the Number Distribution LDS. The density-based classification and visualization method, introduced by Ben Ami

166 et al. (2022), requires no preprocessing of the data or the use of machine-learning algorithms and offers an efficient way  
167 to extract statistically meaningful patterns from large lightning datasets. On one hand, it eliminates information about the  
168 stroke ground-contact point and absolute time of incidence, and on the other, it clusters pairs of strokes with similar time  
169 and space interval properties.

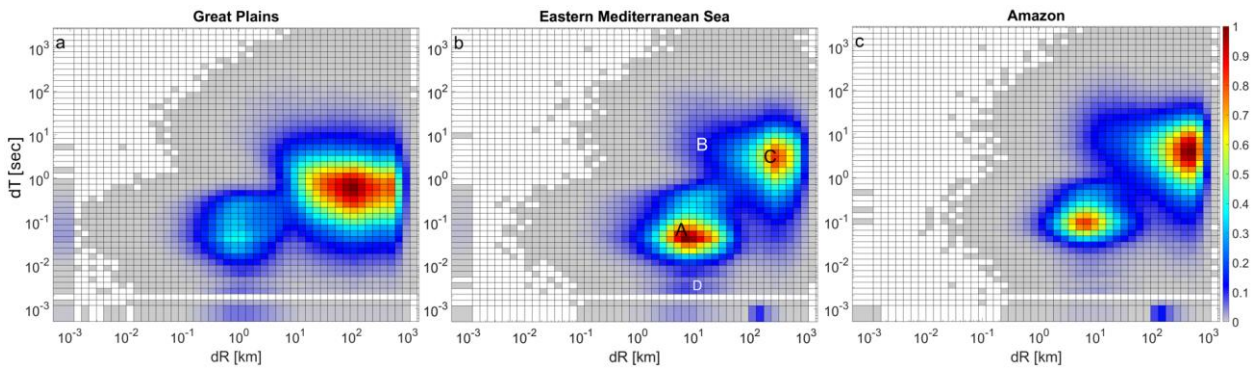
170 To identify interval ranges with a higher likelihood of containing the initial stroke in a flash, we analyzed the peak currents  
171 of consecutive strokes by projecting the ratio of the absolute current value (polarity agnostic) between the 2<sup>nd</sup> and 1<sup>st</sup>  
172 strokes in each pair onto the LDS coordinate system. This approach introduces the Current Ratio LDS. Because peak  
173 currents tend to decrease sequentially within a flash (Chowdhuri et al., 2005), the Current Ratio LDS is used to identify  
174 intervals that are more likely to contain the initial stroke in a flash.

### 175 3. Results and Discussion

176 We first examine the Number Distribution LDS, which provides a statistical view of how stroke intervals populate the  
177 2D dR–dT space. As shown in Fig. 3a–c, stroke intervals with similar dR and dT cluster into distinct "allowed" and  
178 "forbidden" interval ranges, revealing two dominant clusters with a high probability of occurrence. Zero and low count  
179 values reveal the forbidden ranges of dR and dT intervals. This general clustering topography is consistently observed  
180 across all three ROIs. However, shifts in cluster position and variations in cluster characteristics reflect underlying  
181 meteorological differences among the three regions. This 2D representation serves as the reference Number Distribution  
182 LDS, outlining the cluster structure that is examined in detail in the following paragraphs.

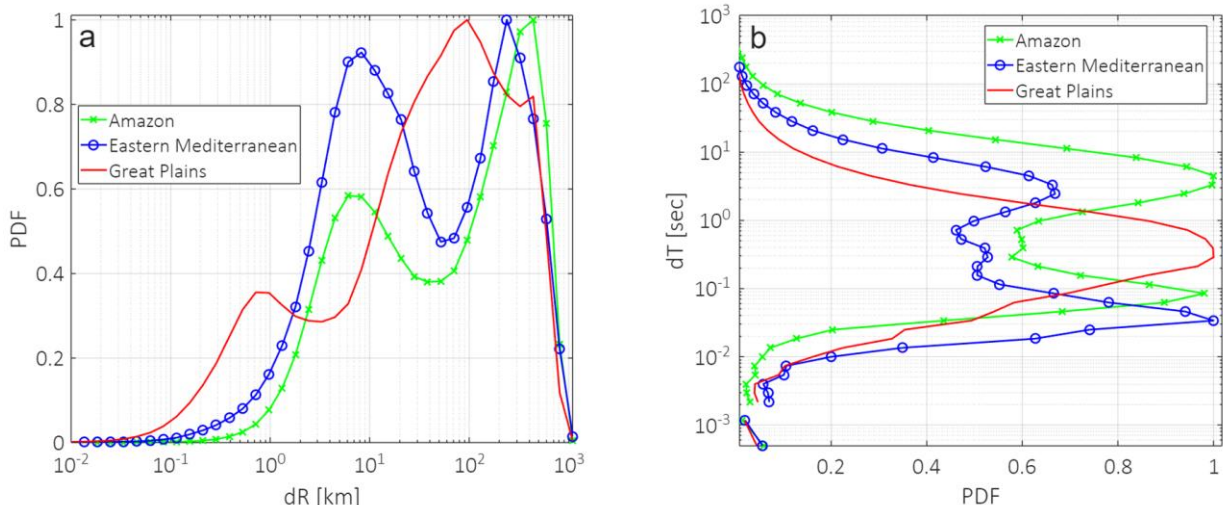
183 The first cluster, marked as A, is characterized by short intervals between successive strokes both in time and space. For  
184 all ROIs, most of the events occur at  $dT < 0.5$  s, and they are limited to dR of a few kilometers and up to a few tens of  
185 kilometers. The second cluster, marked as C, extends over longer dTs and larger dRs. Cluster A represents time and space  
186 intervals between strokes in multiple-stroke flashes (multiplicity  $> 1$ ), as it fits the characteristics of consecutive CG  
187 strokes within a flash (Poelman, 2021; Wu et al., 2020). In contrast, cluster C groups the intervals between the last stroke  
188 in one flash and the initial stroke in the next flash, initiated by a distant thundercloud, in agreement with Ben Ami et al.  
189 (2022). In the case of MCSs, which often span hundreds of kilometers, a subsequent flash may be initiated by a distant  
190 convective cell in the same wide-scale system. Note that the position of cluster C is scale-dependent and is linked to the  
191 area of each ROI. Nevertheless, we chose the areas of the ROIs to be on the order of 500,000 km<sup>2</sup> (Table 1) to cover a  
192 synoptic scale so that the position of cluster C indicates a typical scale of distances between electrical events at a synoptic  
193 (meso) scale.

194 In addition to the two dominant clusters, we identify a ridge-like weak cluster, called here cluster B, representing stroke  
195 intervals between consecutive flashes within a thundercloud. Unlike Ben Ami et al. (2022), who analyzed the ILLS  
196 dataset, cluster B does not exhibit clear centers across all ROIs. This is due to the larger dataset available from the ENTLN  
197 analyzed here and the inclusion of various synoptic conditions. The presence of B in the ENTLN data is illustrated in the  
198 Supplementary Material (Fig. S2) for a smaller dataset. To further validate our findings, we analyzed the ILLS data for  
199 the Eastern Mediterranean (Fig. S1). The results indicate a similar manifestation of B, appearing as a ridge in the Number  
200 Distribution LDS without a distinct center (Fig. S3).



203 Figure 3: Number Distribution LDS. PDF of the  $dR$  and  $dT$  intervals between consecutive strokes, normalized by the maximum, for  
 204 (a) the Great Plains, (b) the Eastern Mediterranean, and (c) the Amazon. The locations of clusters A–D are illustrated in panel (b).  
 205 Intervals with  $PDF < 0.025$  are marked in gray.

206 Figure 4 shows the projection of the PDFs (from Fig. 3) onto the  $dR$  (X) and  $dT$  (Y) axes. The projection on the  $dT$  axis  
 207 (Fig. 4b) clarifies that in the Great Plains, there is no temporal separation between clusters A and C, i.e., between events  
 208 occurring at the cloud scale and at the cloud-system scale. This contrasts with the well-defined temporal separation  
 209 between clusters A and C observed in the other two regions, the Eastern Mediterranean and the Amazon. This lack of  
 210 separation, together with the relatively shorter  $dTs$  of cluster C (between  $\sim 0.1$ – $2.4$ s), is consistent with the higher CAPE  
 211 values and deeper clouds in the Great Plains, which support stronger updrafts and enhanced charge separation, leading to  
 212 shorter stroke-to-stroke intervals. It is also reflected in the high flash density in this region ( $0.037 \text{ km}^{-2} \text{ day}^{-1}$ , Table 1),  
 213 about three times greater than the flash density in the Eastern Mediterranean and the Amazon ( $0.013 \text{ km}^{-2} \text{ day}^{-1}$ , Table 1).  
 214 This finding is supported by Kastman et al. (2017), who report a high CG flash rate for a certain type of MCSs passing  
 215 over the Great Plains during this season. The elevated flash density in this region is likely related to the frequent  
 216 occurrence of MCSs and other long-lived mesoscale systems, which are characterized by a high frequency of electrical  
 217 events and hence shorter intervals between flashes.

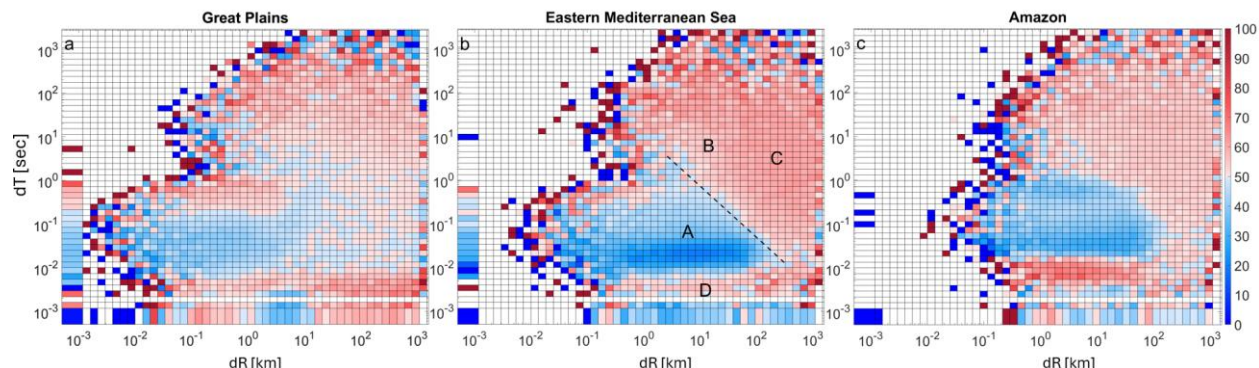


220 Figure 4: Projections of the Number Distribution LDS in Fig. 3 onto the  $dR$  (a) and  $dT$  (b) axes.  
 221

222 Additional differences between the ROIs can be recognized when examining the clusters' positions along the dR axis.  
 223 While in the Amazon and the Eastern Mediterranean, cluster C is centered around 250–400 km, in the Great Plains it is  
 224 located at a shorter distance of ~100 km (Fig. 3 and Fig. 4a). This indicates a smaller characteristic distance, at the cloud-  
 225 system scale, between electrical events in the Great Plains. In addition, the characteristic dR of cluster A is different: it is  
 226 located around 7 km in the Eastern Mediterranean and the Amazon and around 1 km in the Great Plains, suggesting a  
 227 smaller, denser ground-impact radius of strokes within a flash. Poelman et al. (2021) observed a similar tendency for  
 228 shorter distances between ground-strike points within a flash over the U.S. (Florida) when compared with a few other  
 229 regions in Europe, Brazil, and South Africa. Their reported median value of 1.3 km is comparable to our findings for the  
 230 Great Plains. Nevertheless, we cannot rule out that this is a manifestation of smaller location errors over the Great Plains  
 231 due to the higher density of ENTLN sensors in the U.S. The denser sensor coverage in this region results in better detection  
 232 accuracy and improved spatial resolution, which could contribute to the shorter dR values observed in cluster A (Fig. 3–  
 233 4).

234 Using the Current Ratio LDS introduced in Sect. 2.3, we analyze the projection of consecutive strokes' peak current ratio  
 235 onto the LDS coordinate system (Fig. 5). Given that statistically the peak current of CG strokes decreases monotonically  
 236 with their order within a flash, we identify interval ranges that are more likely to represent the initial stroke in a flash (see  
 237 schematic illustration in Fig. S4). Complementary to the Number Distribution LDS in Fig. 3, we find that the Current  
 238 Ratio LDS functions as a partitioning algorithm rather than a clustering method. It separates the space into dR and dT  
 239 interval ranges, in which the current amplitude of the succeeding stroke is statistically larger (reddish) or smaller (bluish)  
 240 than that of the preceding one. In agreement with the interpretation of the clusters in the number-distribution LDS, the 2<sup>nd</sup>  
 241 stroke in a pair in clusters B and C is more likely to have a stronger peak current (reddish) and is therefore assumed to be  
 242 the initial stroke in a new flash. Accordingly, in cluster A, representing consecutive strokes in multiple-stroke CG flashes,  
 243 the 2<sup>nd</sup> stroke in a pair is more likely to have a smaller peak current (bluish).

244



245  
 246 Figure 5: Current Ratio LDS (based on the ratio between the absolute peak current of 2<sup>nd</sup> and 1<sup>st</sup> strokes in each pair) for (a) the Great  
 247 Plains, (b) the Eastern Mediterranean, and (c) the Amazon. Reddish intervals indicate a stronger amplitude of the 2<sup>nd</sup> stroke in more  
 248 than 50% of the pairs, while the bluish intervals show the opposite. The location of clusters A–D is illustrated on panel b. The boundary  
 249 between the main reddish and bluish regions is illustrated by the dashed line in panel b.

250

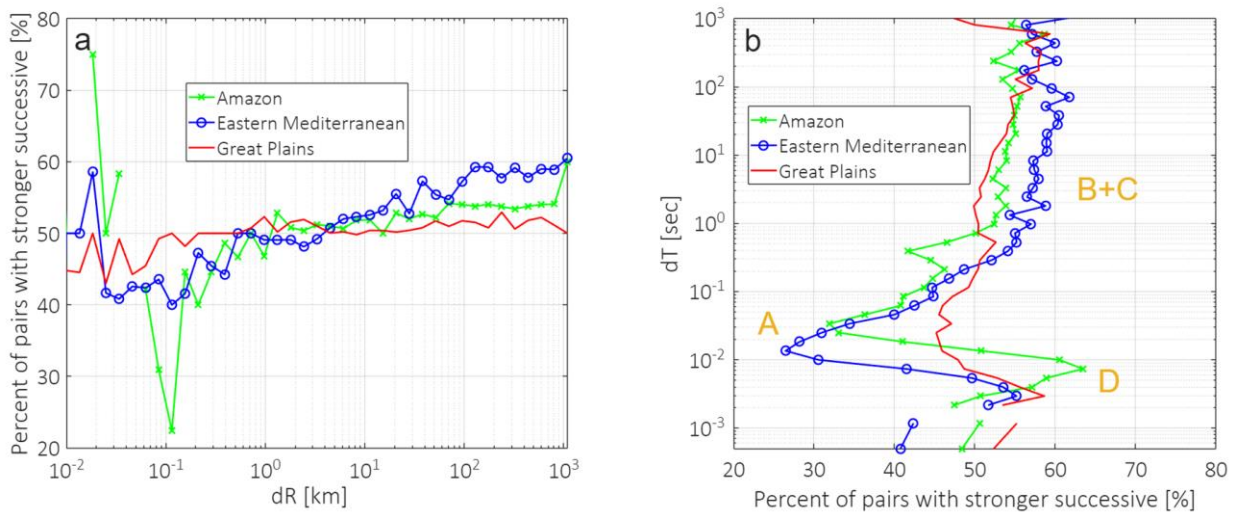
251 This clear and sharp separation into distinct red and blue regions on the Current Ratio LDS is consistent and repeatable  
 252 across the three ROIs, although it is less distinct in the Great Plains. A similar separation between initial and successive  
 253 strokes within a flash, again forming red and blue zones, can be seen in the Current Ratio LDS produced from the ILLS

254 network data (Fig. S5), which is used as a validation dataset. The agreement between the two independent detection  
 255 systems supports the robustness of our findings and indicates that this is a consistent property of lightning discharge  
 256 sequences in thunderstorms.

257 The diagonal boundary between events is illustrated in Fig. 5b. It is not a strict physical boundary but a statistical partition  
 258 that reflects the dominant stroke-pair dynamics: initial strokes (reddish) vs. inter-flash (subsequent) strokes (bluish). It  
 259 indicates that the shorter the distance between strokes, the longer the delay to the next flash. Focusing on time scales of  
 260 a few seconds and distances of a few tens of kilometers, Zoghzogh et al. (2013) reported a similar inverse relation  
 261 between the distance and the time to the next stroke. Here, we demonstrate that this relationship may also apply on a sub-  
 262 second time scale and across tens of kilometers.

263 Analogous to how Fig. 4 summarizes the Number Distribution LDS in Fig. 3, Fig. 6 provides one-dimensional summaries  
 264 that clarify the patterns seen in the two-dimensional current-ratio LDS in Fig. 5. Because the current-ratio is not additive,  
 265 these summaries are computed as the median value along each axis rather than as projections. They highlight how the  
 266 likelihood of a stronger/weaker subsequent stroke varies systematically with distance (Fig. 6a) and time interval (Fig. 6b)  
 267 and demonstrate the contrasting behavior of cluster A versus clusters B and C more clearly.

268 A unique and new feature that appears in the Current Ratio LDS of the three ROIs is cluster D (marked in Fig. 5b and  
 269 6b). This cluster is characterized by very short dTs (on the order of <0.02 s), which are shorter than the characteristic dT  
 270 of cluster A, and a very wide range of dRs, ranging from hundreds of meters to hundreds of kilometers. Containing less  
 271 than 2% of the data, cluster D is not distinct when examining the number of events on the Number Distribution LDS (Fig.  
 272 3). Its topography becomes visible only when examining the Current Ratio LDS (Fig. 5).



273  
 274 Figure 6: Median Current Ratio LDS projected onto the dR (a) and dT (b) axes, respectively, corresponding to the two-dimensional  
 275 distributions shown in Fig. 5a–c. The position of cluster A–D is indicated in panel b.

276  
 277 The validation analysis, similar to the main analysis but using the ILLS network data, reveals a similar cluster D (Fig.  
 278 S5). This supports the robustness of this finding and eliminates the possibility that cluster D is an artifact of the ENTLN  
 279 retrieval algorithm.

280 The high percentage of a stronger peak current of the 2<sup>nd</sup> stroke in a pair in cluster D (similar to clusters B and C, also  
 281 marked in Fig. 6b) indicates that these stroke pairs are probably the initial strokes in flashes. However, cluster D spans a

282 wide range of distances (dRs). For short distances, up to ten or a few tens of kilometers, it may indicate electrical events  
283 within the same thundercloud. It appears when a consecutive stroke in a multiple-stroke flash is more intense than the  
284 previous one, as expected for ~30% of flashes (Diendorfer et al., 2022). In this regard, it is notable that the clustering of  
285 such events occurs at shorter dTs than the typical inter-stroke dT intervals in cluster A. The part of cluster D that pertains  
286 to much longer dRs indicates electrical events involving two strokes that take place nearly simultaneously but at locations  
287 that are tens to hundreds of kilometers apart. Although the exact mechanism is yet to be elucidated, several processes  
288 have been proposed, suggesting that their nearly simultaneous occurrence is not a pure coincidence and that there is a  
289 physical mechanism that ties these remote strokes together. Füllekrug (1995), Ondrášková et al. (2008), and Yair et al.  
290 (2006) have suggested triggering by the Schumann resonance. Later, Yair et al. (2009a) proposed a theoretical model in  
291 which a lightning flash may enhance the electric field in neighboring cells as a function of the distance between them,  
292 potentially triggering a near-simultaneous flash in a remote (mature) thundercloud. Here, using only data from a lightning  
293 location network, we cannot confirm or rule out the lightning-triggering mechanisms that may explain the part of cluster  
294 D with longer dRs.

#### 295 **4. Summary**

296 This study focuses on the parameters of CG flashes within individual thunderclouds and cloud systems. We analyzed the  
297 distribution of stroke intervals as expressed within the Lightning Differential Space (LDS), using both the Number  
298 Distribution LDS (Ben Ami et al., 2022) and the newly introduced Current Ratio LDS. Three distinct climatic regions  
299 were examined: the tropics (Amazon), the subtropics (Eastern Mediterranean Sea), and the mid-latitudes (Great Plains in  
300 the U.S.).

301 By clustering similar events, the Number Distribution LDS enables differentiation between electrical events on the scale  
302 of a single thundercloud versus those of a larger cloud system. The identified clusters represent initial strokes in individual  
303 thunderclouds (ridge B), initial strokes in a cloud system (cluster C), and successive strokes in multi-stroke flashes (cluster  
304 A).

305 The Current Ratio LDS provides an additional key diagnostic tool. It sharply and consistently discriminates between  
306 interval ranges that are more likely to contain initial strokes in flashes and those that are not. A fourth cluster (cluster D)  
307 indicates occurrences of successive strokes striking the ground up to tens to hundreds of kilometers apart, yet within just  
308 a few milliseconds of each other, suggesting possible long-range interaction between thunderstorms. In the present study,  
309 we focus on CG lightning strokes because the characteristic times of IC lightning differ, and hence the application of the  
310 LDS framework to this type of data requires further investigation in future work.

311 Overall, the LDS provides a scalable and objective framework for analyzing large lightning datasets and interpreting their  
312 multiscale nature. It reveals coherent spatiotemporal patterns and regional similarities in flash behavior. These capabilities  
313 support scientific and operational applications, such as comparison with cloud-resolving model outputs and lightning-  
314 parameterization schemes, and the provision of a diagnostic approach that may support probabilistic flash nowcasting or  
315 early-warning tools.

316

317

318 **Code availability**

319 The code used in this study is not publicly available, as it depends on proprietary lightning stroke data that are not  
320 openly accessible. As such, the code cannot be executed or validated independently without access to the licensed  
321 datasets.

322 **Data availability**

323 The lightning stroke data used in this study were obtained from commercial sources under license and are not publicly  
324 available. Access to these data is restricted by data use agreements with the Earth Networks Total Lightning Network  
325 (ENTLN) and the Israel Lightning Location System (ILLs).

326 **Interactive computing environment**

327 No interactive computing environment is available for this study.

328 **Sample availability**

329 No physical samples were used or generated in this study.

330 **Author contribution**

331 IK and YBA develop the concept and the method. YBA performed the analysis. YY provided the datasets. YBA, OA,  
332 YY and IK, wrote the manuscript.

333 **Competing interests**

334 The contact author has declared that none of the authors has any competing interests.

335 **Disclaimer**

336 The views and conclusions expressed in this article are solely those of the authors and do not necessarily reflect the views  
337 of the data providers. The authors have no financial or commercial interest in the data sources used in this study.

338 **Acknowledgement**

339 N/A

340 **Financial support**

341 This project has received funding from the European Research Council (ERC) under the European Union's Horizon 2020  
342 research and innovation programme (grant agreement No 810370), and YY was supported by the Israeli Science  
343 Foundation grant ISF 1848/20.

344 **Review statement**

345 This paper is currently under review for the journal Atmospheric Measurement Techniques.

346 **References**

347 1. Altaratz, O., Levin, Z. and Yair, Y.: Winter thunderstorms in Israel: A study with lightning location systems and  
348 weather radar. Monthly weather review, 129(5), pp.1259-1266, [https://doi.org/10.1175/1520-0493\(2001\)129%3C1259:WTIIAS%3E2.0.CO;2](https://doi.org/10.1175/1520-0493(2001)129%3C1259:WTIIAS%3E2.0.CO;2), 2001.

350 2. Altaratz, O., Levin, Z., Yair, Y., and Ziv, B.: Lightning activity over land and sea on the eastern coast of the  
351 Mediterranean, *Monthly Weather Review* 131, no. 9, 2060-2070, [https://doi.org/10.1175/1520-0493\(2003\)131<2060:LAOLAS>2.0.CO;2](https://doi.org/10.1175/1520-0493(2003)131<2060:LAOLAS>2.0.CO;2), 2003.

353 3. Andreae, M.O., Rosenfeld, D., Artaxo, P., Costa, A.A., Frank, G.P., Longo, K.M. and Silva-Dias, M.A.F.D.:  
354 Smoking rain clouds over the Amazon. *science*, 303(5662), pp.1337-1342,  
355 <https://doi.org/10.1126/science.1092779>, 2004.

356 4. Ben Ami, Y., Altaratz, O., Yair, Y. and Koren, I.: Lightning characteristics over the eastern coast of the  
357 Mediterranean during different synoptic systems. *Natural Hazards and Earth System Sciences*, 15(11), pp.2449-  
358 2459, <https://doi.org/10.5194/nhess-15-2449-2015>, 2015.

359 5. Ben Ami, Y., Altaratz, O., Koren, I., and Yair, Y.: Allowed and forbidden zones in a Lightning-strokes spatio-  
360 temporal differential space, *Environmental Research Communications*, 4(3), p.031003, DOI 10.1088/2515-  
361 7620/ac5ec2, 2022.

362 6. Carey, L.D. and Rutledge, S.A.: The relationship between precipitation and lightning in tropical island  
363 convection: A C-band polarimetric radar study. *Monthly weather review*, 128(8), pp.2687-2710,  
364 [https://doi.org/10.1175/1520-0493\(2000\)128%3C2687:TRBPAL%3E2.0.CO;2](https://doi.org/10.1175/1520-0493(2000)128%3C2687:TRBPAL%3E2.0.CO;2), 2000.

365 7. Carvalho, L.M., Jones, C. and Liebmann, B: The South Atlantic convergence zone: Intensity, form, persistence,  
366 and relationships with intraseasonal to interannual activity and extreme rainfall, *Journal of Climate*, 17(1), pp.88-  
367 108., [https://doi.org/10.1175/1520-0442\(2004\)017%3C0088:TSACZI%3E2.0.CO;2](https://doi.org/10.1175/1520-0442(2004)017%3C0088:TSACZI%3E2.0.CO;2), 2004.

368 8. Chowdhuri, P., Anderson, J.G., Chisholm, W.A., Field, T.E., Ishii, M., Martinez, J.A., Marz, M.B., McDaniel,  
369 J., McDermott, T.E., Mousa, A.M., and Narita, T.: Parameters of lightning strokes: A review. *IEEE Transactions  
370 on Power Delivery*, 20(1), pp.346-358, doi:10.1109/TPWRD.2004.835039, 2005.

371 9. Collow, A.B.M., Miller, M.A. and Trabachino, L.C.: Cloudiness over the Amazon rainforest: Meteorology and  
372 thermodynamics. *Journal of Geophysical Research: Atmospheres*, 121(13), pp.7990-8005,  
373 <https://doi.org/10.1002/2016JD024848>, 2016.

374 10. Cotton, W.R., Bryan, G., and van den Heever, S.C.: Cumulonimbus clouds and severe convective storms, In  
375 International geophysics (Vol. 99, pp. 315-454), Academic Press, [https://doi.org/10.1016/S0074-6142\(10\)09914-6](https://doi.org/10.1016/S0074-6142(10)09914-6), 2011.

377 11. Deierling, W., and Petersen, W.A.: Total lightning activity as an indicator of updraft characteristics, *Journal of  
378 Geophysical Research: Atmospheres*, 113(D16), <https://doi.org/10.1029/2007JD009598>, 2008.

379 12. Deierling, W., Petersen, W.A., Latham, J., Ellis, S., and Christian, H.J.: The relationship between lightning  
380 activity and ice fluxes in thunderstorms, *Journal of Geophysical Research, Atmospheres*, 113(D15),  
381 <https://doi.org/10.1029/2007JD009700>, 2008.

382 13. Dwyer, J.R., and Uman, M.A.: The physics of lightning, *Physics Reports*, 534(4), pp.147-241,  
383 <http://dx.doi.org/10.1016/j.physrep.2013.09.004>, 2014.

384 14. Diendorfer, G., Bologna, F.F., and Engelbrecht, C.S.: A review of the relationship between peak currents of the  
385 first and subsequent strokes in the same flash, In 2022 36th International Conference on Lightning Protection  
386 (ICLP) (pp. 10-13), IEEE, <https://doi.org/10.1109/ICLP56858.2022.9942502>, 2022.

387 15. Füllekrug, M.: Schumann resonances in magnetic field components, *Journal of Atmospheric and Terrestrial  
388 Physics*, 57(5), pp.479-484, [https://doi.org/10.1016/0021-9169\(94\)00075-Y](https://doi.org/10.1016/0021-9169(94)00075-Y), 1995.

389 16. Giangrande, S.E., Feng, Z., Jensen, M.P., Comstock, J.M., Johnson, K.L., Toto, T., Wang, M., Burleyson, C.,  
390 Bharadwaj, N., Mei, F. and Machado, L.A.: Cloud characteristics, thermodynamic controls and radiative impacts  
391 during the Observations and Modeling of the Green Ocean Amazon (GoAmazon2014/5)  
392 experiment. *Atmospheric Chemistry and Physics*, 17(23), pp.14519-14541, <https://doi.org/10.5194/acp-17-14519-2017>, 2017.

394 17. Gizaw, M.S., Gan, T.Y., Yang, Y. and Gan, K.E. Changes to the 1979–2013 summer convective available  
395 potential energy (CAPE) and extreme precipitation over North America. *Physics and Chemistry of the Earth,  
396 Parts A/B/C*, 123, p.103047, <https://doi.org/10.1016/j.pce.2021.103047>, 2021.

397 18. Harris Jr, G.N., Bowman, K.P. and Shin, D.B.: Comparison of freezing-level altitudes from the NCEP reanalysis  
398 with TRMM precipitation radar brightband data. *Journal of climate*, 13(23), pp.4137-4148, 2000.

399 19. Higgins, R.W., Yao, Y., Yarosh, E.S., Janowiak, J.E., and Mo, K.C.: Influence of the Great Plains low-level jet  
400 on summertime precipitation and moisture transport over the central United States, *Journal of Climate*, 10(3),  
401 pp.481-507, [https://doi.org/10.1175/1520-0442\(1997\)010%3C0481:IOTGPL%3E2.0.CO;2](https://doi.org/10.1175/1520-0442(1997)010%3C0481:IOTGPL%3E2.0.CO;2), 1997.

402 20. Jiang, X., Lau, N.C. and Klein, S.A.: Role of eastward propagating convection systems in the diurnal cycle and  
403 seasonal mean of summertime rainfall over the US Great Plains. *Geophysical Research Letters*, 33(19),  
404 <https://doi.org/10.1029/2006GL027022>, 2006.

405 21. Kaplan, J.O., and Lau, K.H.K.: World wide lightning location network (WWLLN) global lightning climatology  
406 (WGLC) and time series, 2022 update, *Earth System Science Data*, 14(12), pp.5665-5670,  
407 <https://doi.org/10.5281/zenodo.6007052>, 2022.

408 22. Kastman, J.S., Market, P.S., Fox, N.I., Foscato, A.L., and Lupo, A.R.: Lightning and rainfall characteristics in  
409 elevated vs. surface based convection in the midwest that produce heavy rainfall, *Atmosphere*, 8(2), p.36,  
410 <https://doi.org/10.3390/atmos8020036>, 2017.

411 23. Katz, E. and Kalman, G.: The impact of environmental and geographical conditions on lightning parameters  
412 derived from lightning location system in Israel, In Proceeding of the 10th International Symposium on Lightning  
413 Protection, Curitiba, Brazil, November (pp. 9-13), 2009.

414 24. MacGorman, D.R., and Rust, W.D.: *The electrical nature of storms*, Oxford University Press, USA, 1998.

415 25. Maddox, R.A., Howard, K.W., Bartels, D.L., and Rodgers, D.M.: Mesoscale convective complexes in the middle  
416 latitudes, In *Mesoscale meteorology and forecasting* (pp. 390-413), Boston, MA: American Meteorological  
417 Society, 1986.

418 26. Mattos, E.V., and Machado, L.A.: Cloud-to-ground lightning and Mesoscale Convective Systems, Atmospheric  
419 Research, 99(3-4), pp.377-390, <https://doi.org/10.1016/j.atmosres.2010.11.007>, 2011.

420 27. Mazur, V: Associated lightning discharges, Geophysical Research Letters, 9(11), pp.1227-1230,  
421 <https://doi.org/10.1029/GL009i011p01227>, 1982.

422 28. Molion, L.C.B.: Amazonia rainfall and its variability, Hydrology and water management in the humid tropics,  
423 Hufschmidt, M.M., Gladwell, J.S., Eds., pp.99-111, 1993.

424 29. Nobre, C.A., Obregón, G.O., Marengo, J.A., Fu, R., and Poveda, G.: Characteristics of Amazonian climate: main  
425 features, Amazonia and global change, 186, pp.149-162, 2009.

426 30. Oda, P.S., Enoré, D.P., Mattos, E.V., Gonçalves, W.A., and Albrecht, R.I.: An initial assessment of the  
427 distribution of total Flash Rate Density (FRD) in Brazil from GOES-16 Geostationary Lightning Mapper (GLM)  
428 observations, Atmospheric Research, 270, p.106081, <https://doi.org/10.1016/j.atmosres.2022.106081>, 2022.

429 31. Ondrášková, A., Bór, J., Kostecký, P., and Rosenberg, L.: Peculiar transient events in the Schumann resonance  
430 band and their possible explanation, Journal of atmospheric and solar-terrestrial physics, 70(6), pp.937-946,  
431 <https://doi.org/10.1016/j.jastp.2007.04.013>, 2008.

432 32. Poelman, D.R., Schulz, W., Pedeboy, S., Hill, D., Saba, M., Hunt, H., Schwalt, L., Vergeiner, C., Mata, C.,  
433 Schumann, C., and Warner, T.: Global ground strike point characteristics in negative downward lightning  
434 flashes—Part 1: Observations, Natural Hazards and Earth System Sciences Discussions, 2021, pp.1-17,  
435 <https://doi.org/10.5194/nhess-21-1909-2021>, 2021.

436 33. Rakov, V.A., A review of positive and bipolar lightning discharges, Bulletin of the American Meteorological  
437 Society, 84(6), pp.767-776, <https://doi.org/10.1175/BAMS-84-6-767>, 2003.

438 34. Riemann-Campe, K., Fraedrich, K. and Lunkeit, F.: Global climatology of convective available potential energy  
439 (CAPE) and convective inhibition (CIN) in ERA-40 reanalysis. Atmospheric Research, 93(1-3), pp.534-545,  
440 <https://doi.org/10.1016/j.atmosres.2008.09.037>, 2009.

441 35. San Segundo, H., López, J.A., Pineda, N., Altube, P. and Montanya, J.: Sensitivity analysis of lightning stroke-  
442 to-flash grouping criteria. Atmospheric Research, 242, pp.105023,  
443 <https://doi.org/10.1016/j.atmosres.2020.105023>, 2020.

444 36. Scuff, L., Prein, A.F., Li, Y., Clark, A.J., Krogh, S.A., Taylor, N., Liu, C., Rasmussen, R.M., Ikeda, K., and Li,  
445 Z., Dryline characteristics in North America's historical and future climates, Climate Dynamics, 57(7), pp.2171-  
446 2188, <https://doi.org/10.1007/s00382-021-05862-1>, 2021.

447 37. Setvák, M., Lindsey, D.T., Novák, P., Wang, P.K., Radová, M., Kerkmann, J., Grasso, L., Su, S.H., Rabin, R.M.,  
448 Šťástka, J. and Charvát, Z.: Satellite-observed cold-ring-shaped features atop deep convective clouds.  
449 Atmospheric Research, 97(1-2), pp.80-96, <https://doi.org/10.1016/j.atmosres.2010.03.009>, 2010.

450 38. Shalev, S., Saaroni, H., Izsak, T., Yair, Y., and Ziv, B.: The spatio-temporal distribution of lightning over Israel  
451 and the neighboring area and its relation to regional synoptic systems, Natural Hazards and Earth System  
452 Sciences, 11(8), pp.2125-2135, <https://doi.org/10.5194/nhess-11-2125-2011>, 2011.

453 39. Shay-El, Y. and Alpert, P.: A diagnostic study of winter diabatic heating in the Mediterranean in relation to  
454 cyclones. *Quarterly Journal of the Royal Meteorological Society*, 117(500), pp.715-747,  
455 <https://doi.org/10.1002/qj.49711750004>, 1991.

466 40. Siingh, D., Gopalakrishnan, V., Singh, R.P., Kamra, A.K., Singh, S., Pant, V., Singh, R., and Singh, A.K. :The  
467 atmospheric global electric circuit: an overview, *Atmospheric Research*, 84(2), pp.91-110,  
468 <https://doi.org/10.1016/j.atmosres.2006.05.005>, 2007.

469 41. Strauss, C., Rosa, M.B. and Stephany, S.: Spatio-temporal clustering and density estimation of lightning data for  
470 the tracking of convective events, *Atmospheric Research*, 134, pp.87-9,  
471 <https://doi.org/10.1016/j.atmosres.2013.07.008>, 2013.

472 42. Tuttle, J.D. and Davis, C.A.: Corridors of warm season precipitation in the central United States, *Monthly  
473 Weather Review*, 134(9), pp.2297-2317, <https://doi.org/10.1175/MWR3188.1>, 2006.

474 43. Vonnegut, B., Vaughan Jr, O.H., Brook, M., and Krehbiel, P.: Mesoscale observations of lightning from space  
475 shuttle, *Bulletin of the American Meteorological Society*, 66(1), pp.20-29, [https://doi.org/10.1175/1520-0477\(1985\)066%3C0020:MOOLFS%3E2.0.CO;2](https://doi.org/10.1175/1520-0477(1985)066%3C0020:MOOLFS%3E2.0.CO;2), 1985.

476 44. Wiens, K. C., and Suszcynsky, D. M.: Observed relationships among Narrow Bipolar Events, total lightning and  
477 convective strength in Summer 2005 Great Plains thunderstorms. *Second Conference on Meteorological  
478 Applications of Lightning Data*, AMS Annual Meeting, Poster P1.8, 2006.

479 45. Williams, E., Rosenfeld, D., Madden, N., Gerlach, J., Gears, N., Atkinson, L., Dunnemann, N., Frostrom, G.,  
480 Antonio, M., Biazon, B., and Camargo, R.: Contrasting convective regimes over the Amazon: Implications for  
481 cloud electrification, *Journal of Geophysical Research: Atmospheres*, 107(D20), pp.LBA-50,  
482 <https://doi.org/10.1029/2001JD000380>, 2002.

483 46. Wright, J.S., Fu, R., Worden, J.R., Chakraborty, S., Clinton, N.E., Risi, C., Sun, Y., and Yin, L.: Rainforest-  
484 initiated wet season onset over the southern Amazon, *Proceedings of the National Academy of Sciences*, 114(32),  
485 pp.8481-8486, <https://doi.org/10.1073/pnas.1621516114>, 2017.

486 47. Wu, T., Wang, D., and Takagi, N.: Multiple-stroke positive cloud-to-ground lightning observed by the FALMA  
487 in winter thunderstorms in Japan, *Journal of Geophysical Research: Atmospheres*, 125(20), p.e2020JD033039,  
488 <https://doi.org/10.1029/2020JD033039>, 2020.

489 48. Yair, Y., Aviv, R., Ravid, G., Yaniv, R., Ziv, B., and Price, C.: Evidence for synchronicity of lightning activity  
490 in networks of spatially remote thunderstorms, *Journal of atmospheric and solar-terrestrial physics*, 68(12),  
491 pp.1401-1415, <https://doi.org/10.1016/j.jastp.2006.05.012>, 2006.

492 49. Yair, Y.Y., Aviv, R., and Ravid, G.: Clustering and synchronization of lightning flashes in adjacent  
493 thunderstorm cells from lightning location networks data, *Journal of Geophysical Research: Atmospheres*,  
494 114(D9), <https://doi.org/10.1029/2008JD010738>, 2009a.

486 50. Yair, Y., Price, C., Ganot, M., Greenberg, E., Yaniv, R., Ziv, B., Sherez, Y., Devir, A., Bór, J.Z. and Sátori, G.:  
487 Optical observations of transient luminous events associated with winter thunderstorms near the coast of Israel.  
488 Atmospheric Research, 91(2-4), pp.529-537, <https://doi.org/10.1016/j.atmosres.2008.06.018>, 2009b.

489 51. Yair, Y.: Lightning hazards to human societies in a changing climate, Environmental research letters, 13(12),  
490 p.123002, DOI 10.1088/1748-9326/aaea86, 2018.

491 52. Zhu, Y., Stock, M., Lapierre, J., and DiGangi, E.: Upgrades of the Earth networks total lightning network in  
492 2021, Remote sensing, 14(9), p.2209, <https://doi.org/10.3390/rs14092209>, 2022.

493 53. Ziegler, C.L., and Rasmussen, E.N.: The initiation of moist convection at the dryline: forecasting issues from a  
494 case study perspective, Weather and forecasting, 13(4), pp.1106-1131, [https://doi.org/10.1175/1520-0434\(1998\)013%3C1106:TIOMCA%3E2.0.CO;2](https://doi.org/10.1175/1520-0434(1998)013%3C1106:TIOMCA%3E2.0.CO;2), 1998.

496 54. Ziv, B., Dayan, U., and Sharon, D.: A mid-winter, tropical extreme flood-producing storm in southern Israel:  
497 synoptic scale analysis, Meteorology and Atmospheric Physics, 88, pp.53-63, <https://doi.org/10.1007/s00703-003-0054-7>, 2005.

499 55. Zoghzoghy, F.G., Cohen, M.B., Said, R.K., and Inan, U.S.: Statistical patterns in the location of natural lightning,  
500 Journal of Geophysical Research: Atmospheres, 118(2), pp.787-796, <https://doi.org/10.1002/jgrd.50107>, 2013.